https://doi.org/10.26168/ajce.41.4.6

Spatial variability of concrete resistivity as a function of vibration and time

Yanyan XIAO[1], **Romain CLERC**[1], **Franck SCHOEFS**[1], **Wael KARAM**[1], **Yann LECIEUX**[1], **Mathilde CHEVREUIL**[1], **Magda-Marcela TORRES-LUQUE**[1]

[1] *Nantes Université, École Centrale Nantes, CNRS, GeM, UMR 6183, F-44000 Nantes, France*

ABSTRACT Spatial variability of concrete resistivity is a key element for optimal design of embedded resistivity sensors, which allow to catch chloride ions propagation in concrete structures. Its temporal evolution and its dependence on the vibration protocol remains however unknown. In this paper, we address these questions by assessing time-evolution of spatial variability of apparent resistivity of 10 concrete beams realized with two different vibration protocols (needle and table) and placed in a climatic chamber. We find that each beam exhibits (i) a time-independent resistivity spatial signature, and (ii) a periodicity of correlation in space, roughly corresponding to the lag of vibration protocol for both. This suggests time-invariance of resistivity's spatial variability of sound concrete and its strong dependence to vibration protocol.

Mots-clefs variabilité spatiale, résistivité apparente, béton, protocole de vibration, données

Key-words spatial variability, apparent resistivity, concrete, vibration protocol, data

I. INTRODUCTION

It has been shown, over the past 20 years, that knowledge of the spatial variability of concrete properties is a key element of reliability-based maintenance. Moreover, in the last decade, embedded sensors based on resistivity measurements have demonstrated their interest in monitoring concrete curing and monitoring chloride ions penetration (Lecieux et al., 2019), which is a key durability indicator. These sensors consist of electrodes aligned on a PVC support and allow to measure resistivity along a structural component (beam). Their optimal design (length, distance between electrodes) and their optimal distribution pattern in a structure depend on the knowledge of the spatial variability of resistivity, respectively at the component scale and at the structural scale.

To render their spatial variability, concrete properties should thus be considered a priori as Random Fields (RF) instead of random variables. RF are defined by a marginal distribution and a semi-variogram γ, with first one describing variability between similar concrete elements and second one a function describing variability within a single concrete element (Clerc, 2021, para. V; Cressie, 1991). More specifically, as illustrated by its estimator $\hat{\gamma}$ (Equation (1)), γ represents the variance of the difference between two measurements of the same property according to the distance lag h between them. In the following, we note Z a RF defined on a domain D, and $Z(x)$ any of its realizations georeferenced by a vector x, called a trajectory.

$$\hat{\gamma} = \frac{1}{2N_h} \sum_{i=1,\dots,N_h} [Z(x_i) - Z(x_i + h)]^2 \quad (1)$$

https://doi.org/10.26168/ajce.41.4.6

In this paper, we focus on the analysis and assessment of the spatial variability of the resistivity at the component scale through the monitoring of 10 specimens in time. These are realized with two vibration protocols (needle and table), whose comparative effects on spatial variability remain unknown. After introducing the experimental procedure (II) and analyzing raw data to select adapted RF models (III), we detail our methodology for spatial variability assessment of apparent resistivity (IV) and expose our results (V) and conclusions (VI).

II. EXPERIMENTAL PROCEDURE

A. Apparent resistivity measurement

The Wenner method (shown in **Figure 1**) is commonly used for detecting apparent electrical resistivity (ρ) of the subsurface. It involves placing electrodes at fixed intervals (a) and measuring potential differences (V) between testing points. By varying the intervals (a) it allows to measure the apparent resistivity at different layers following Equation (2). In a semi-infinite medium, $K(a) = 2\pi a \times V/I$ whereas it is determined through Finite-Element computation otherwise (du Plooy et al., 2013). Note that for low a values, apparent resistivity is close to true resistivity because of the limited length of current lines.

$$\rho = K(a) \times V/I \tag{2}$$

B. Material and specimens

In the following, we study apparent resistivity data coming from 10 concrete specimens of research project SIMAR. These are made from the same concrete in two different designs, and placed in a climatic chamber. They include embedded Wenner sensors constituted of 32 evenly-distributed electrodes with a 3.5-mm spacing, allowing to measure apparent resistivity at 29 points at a depth of 13.5 mm and at 26 points at a depth of 19.4 mm (**Figure 2**). Both 13.5 and 19.4 mm are low depths at which the true resistivity is close to the apparent resistivity (section II.A).

SIMAR project involves a first set of 9 specimens made on 07/11/2022, labeled from I to Q and monitored over four months. These were poured in a single operation and vibrated using a Ø25 mm vibrating needle with a regular spacing of 175 mm, for 10 seconds at each point (**Figure 3**).

It involves another single specimen, labeled iM made on 03/05/2022 and monitored over ten months. Its formwork's sides were separated by a metal plate in order to cast two similar concretes with different chloride concentrations (60 g/l on one side, no salt on the other). Each of them was poured by 10-cm thick layers vibrated for 20-25 seconds using a Ø25 mm vibrating needle. This was placed under and perpendicular to the formwork support, in the middle of each part (**Figure 4**). This induced vibration of both the formwork and the plate, resulting in a longitudinal vibration spacing of 29 cm. Metal plate was removed after 1.5 hours to keep concrete parts from mixing.

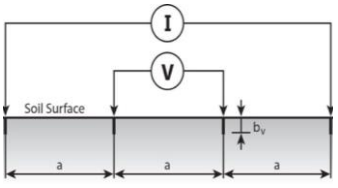

Figure 1. Schematic view of Wenner protocol

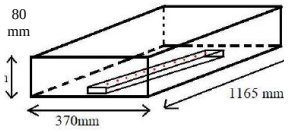

Figure 2. Specimen dimensions

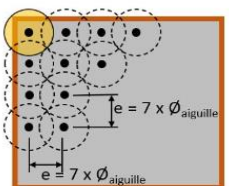

Figure 3. Vibration protocol (I to Q)

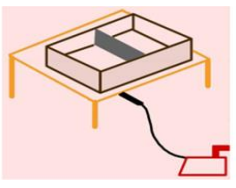

Figure 4. Vibration protocol (spec. iM)

https://doi.org/10.26168/ajce.41.4.6

III. APPARENT RESISTIVITY EVOLUTION

A. Specimen I to Q

Processed apparent resistivity data along specimens I to Q constitute 106 1D apparent resistivity trajectories, for 9 specimens, 6 times and 2 depths. These are plotted in **Figure 5**. Their analysis shows following points: (i) apparent resistivity increases over time due to hydration reactions at both depths, with lower values in the deeper layer ; (ii) trajectories with common depth and time exhibit stationary trends, as previously observed (Priou et al., 2019) ; (iii) mean and variance of apparent resistivity show an increasing trend for common beam and depth, while histogram shapes are closely symmetric and approximate normal distributions. Data can thus be preliminary considered as realizations of unidimensional Gaussian Random Fields (GRF).

B. Specimen iM

Processed apparent resistivity data along specimen iM constitute 20 1D trajectories, for 1 specimen, 10 times and 2 depths. These are plotted in **Figure 6**. Their analysis indicates that data can be preliminary considered as realizations of Trend and Variance-Stationary GRF (noted as TS-VS GRF) with stepwise means and variances.

C. Specimens' signatures

In addition to these observations, plotting of roughly standardized data (with classical mean and variance estimates) reveal that each depth of each specimen has its own *spatial signature*, namely a proper time-invariant apparent resistivity pattern (**Figure 7**). This is in line with observations of (Priou et al., 2019) and lead ourself to focus on the geostatistical study of these spatial signatures.

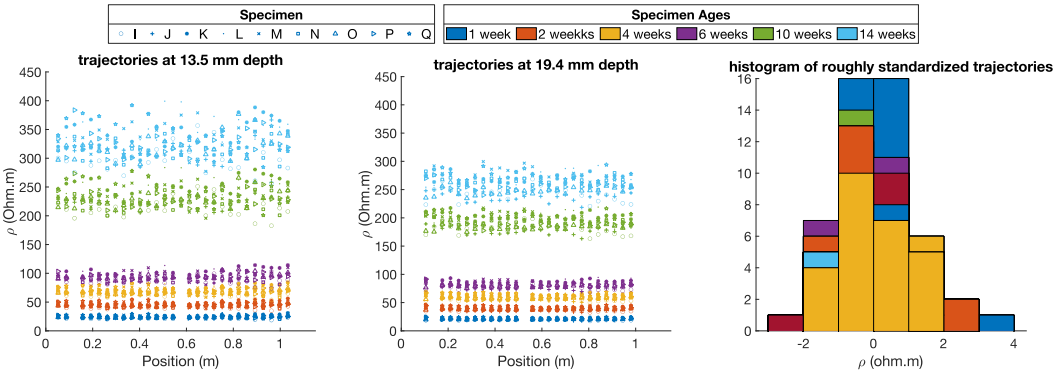

Figure 5. Apparent resistivity trajectories and their histograms (spec. I to Q)

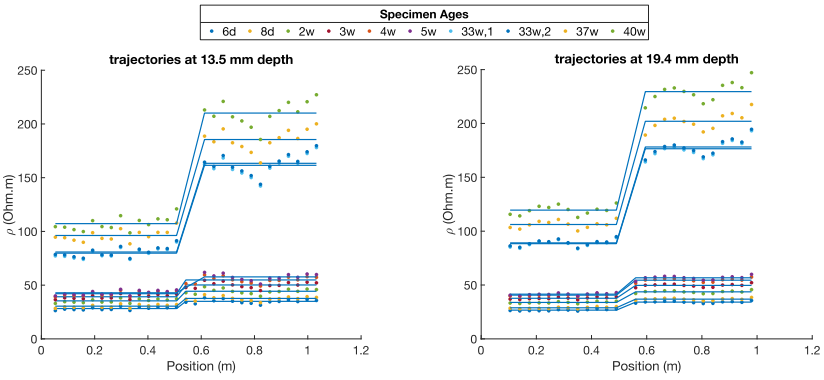

Figure 6. Apparent resistivity trajectories (spec. iM)

https://doi.org/10.26168/ajce.41.4.6

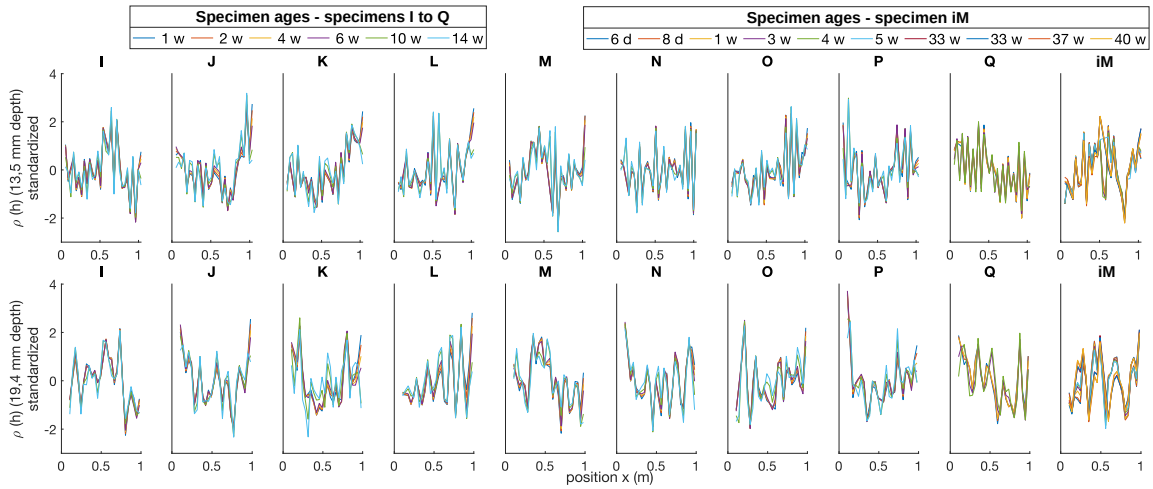

Figure 7. Standardized trajectories of all specimens

IV. SPATIAL VARIABILITY ANALYSIS

A. Empirical semi-variograms

We start spatial variability analysis by plotting empirical semi-variograms of standardized data, following recommendations of (Cressie, 1991, p. 97) (**Figure 8**). As expected, these show same patterns for common specimen and depth along time, with a slight change after one month.

This could result from the vibration protocol, especially the spacing of vibrating needle during pouring. In the following, we investigate this assumption by focusing on geostatistical characterization of standardized trajectories coming from second depth of previously cited specimens. These are called *hole-effect trajectories*. Note however that this behavior is not observed in the 13.5-mm layer. This may be due to the mainly circular action of the vibrating needle as well as the low differences between layer depth, the size of the electrodes and the distance between them, which may affect boundary and add local geometrical effects.

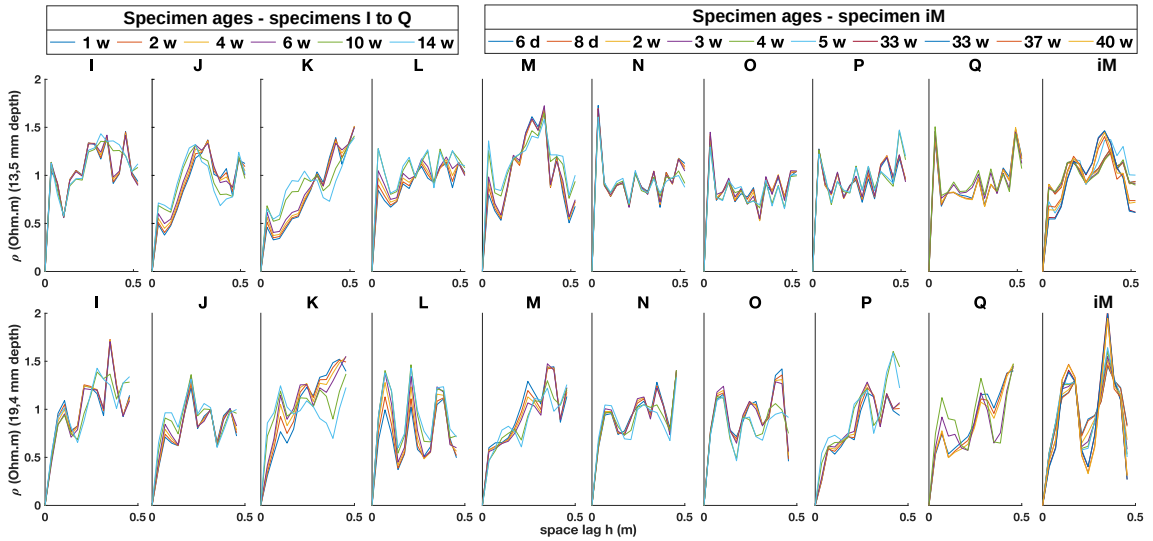

Figure 8. Empirical semi-variograms of standardized trajectories of both projects

https://doi.org/10.26168/ajce.41.4.6

B. Geostatistical characterization of hole-effect trajectories

Purpose of the geostatistical characterization of hole-effect trajectories is to check statistical significance of the observed hole effect by identifying the best semi-variogram models for their RF, and to check its eventual link to the vibration protocol by estimating and comparing their fluctuation parameters. To do so, we follow the SCAP-1D method proposed by (Clerc et al., 2019), illustrated on Erreur ! Source du renvoi introuvable.**Figure 9**, with RF considered as Standard GRF due to previous observations.

In a first time, we perform this process considering trajectories as realizations of independent RF. Statistical significance of the observed spatial signature is then considered only if there is an overlap between confidence intervals (CI) of fluctuation parameters of semi-variograms for common specimen and depth.

In Step 1, we select 4 eventual models for γ, listed in **Table 1**. Models 2, 3 and 4 render hole effect and are selected from (Chilès and Delfiner, 2012; Pyrcz and Deutsch, 2003). Model 1 doesn't render hole effect but is selected to check statistical significance of the observed hole effect. Model 3 and 4 share a common parameter λ, which is the *wavelength* of the correlation. In Model 4 variance of Gaussian part is obtained from variance of cosine part s_2, as both contribute to the unit variance of the Standard GRF.

In Step 2, we estimate parameters for each model through Maximum Likelihood Estimation (MLE) computed from the data (Clerc et al., 2019; Wasserman, 2004). Initial values of the optimization process behind this method are given through weighted Least-Square Estimates (wLSE) made on the empirical semi-variograms (Chilès and Delfiner, 2012).

In Step 3 and 4, we check statistical validity of the standard GRF models and estimates, i.e stationarity and normality of the decorrelated data, as well as trajectories ergodicity, required to perform estimates trajectory per trajectory. To ensure robustness, decorrelation is done with both empirical and modeled covariance matrix (Σ_{exp} and Σ_{mod}). Stationarity test is the KPSS-test (Kwiatkowski et al., 1992), normality tests are the Kolmogorov-Smirnov and the Shapiro-Wilk ones (de Smith, 2018). Ergodicity is checked when semi-variograms show an asymptotic behavior (Cressie, 1991, p. 57).

Table 1. Selected semi-variogram models for the estimation

#	Type	Name	Model	Parameters	Nb of parameters
1	Monotonic	Gaussian	$\gamma/2(h) = 1 - \exp(-(h/a)^2)$	$a > 0$	1
2	Hole effect	Cardinal sine	$\gamma/2(h) = 1 - \sin(h/a)/(h/a)$	$a > 0$	1
3		Damped cosine	$\gamma/2(\mathrm{h}) = 1 - \left(\exp(-\mathrm{q}.\mathrm{h}) \times \cos\left(\frac{2\pi}{\lambda}.\mathrm{h}\right)\right)$	$q, b > 0$	2
4		Gaussian-cosine	$\gamma/2(\mathrm{h}) = (1 - \mathrm{s}_2) \times \left[1 - \exp\left(-\left(\frac{h}{a}\right)^2\right)\right] + \mathrm{s}_2 \times [1 - \cos\left(\frac{2\pi}{\lambda}.\mathrm{h}\right)]$	$s_2, a, b > 0$	3

For each trajectory, identification of the best semi-variogram model is done in two steps: (i) we compute the corrected Akaike Information Criterion (AICc) for each model i (Equ. (3)); (ii) we compare their goodness-of-fit by computing their Evidence Ratios (ER), with a unit value for the best (Equ. (4)). This procedure allows to select the most accurate model that describes the hidden RF in case of few data (Burnham et al., 2010). We note $L(\hat{p}|Z(x))$ the likelihood of hidden RF model with K parameters estimated by MLE ($\hat{p}$), given $Z(x)$ trajectory with n datapoints.

https://doi.org/10.26168/ajce.41.4.6

$$AICc = AIC + \frac{2K(K+1)}{n-K-1} = -2\ln\left(L(\hat{p}|Z)\right) + 2K + \frac{2K(K+1)}{n-K-1} \quad (3)$$

$$ER_i = exp\left(\frac{1}{2}\left[AICc_i - AICc_{jmin}\right]\right) \quad (4)$$

V. RESULTS

A. *Estimations of parameters for each trajectory*

As an illustration of estimation results, we plot on **Figure 10** empirical semi-variograms related to 14 week-aged specimen L, as well as its estimate with the 4 models. As a synthesis of the whole estimations, we plot on **Figure 11** the ERs of each model fit for each hole-effect trajectory. The bars below value of 1 indicate then the best-fit model for each trajectory. This plot clearly shows that models with hole effects have better fit than the monotonic one. We thus plot on **Figure 12** estimates and CIs of wavelength λ only for models 3 and 4.

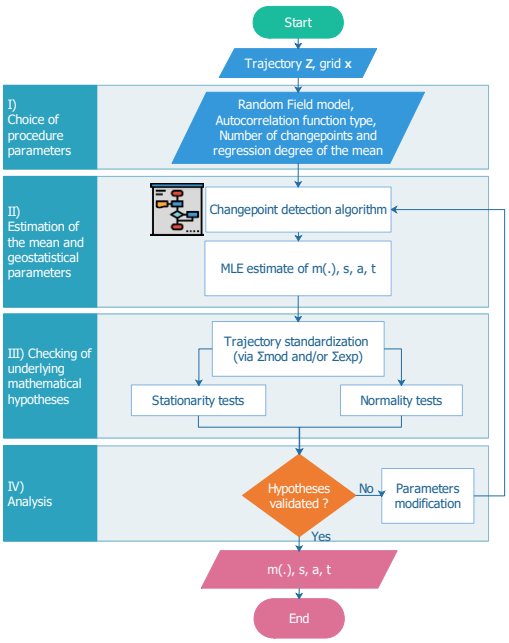

Figure 9 : SCAP-1D flowchart

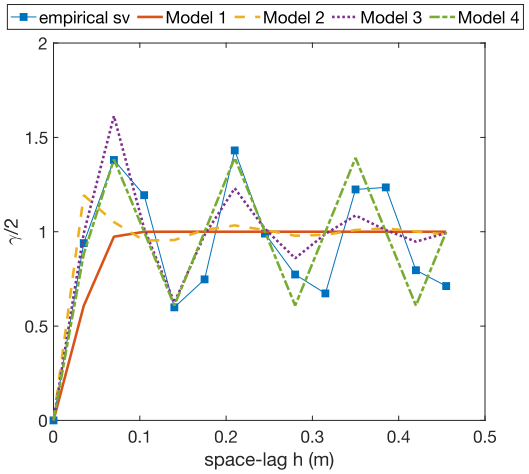

Figure 10. Illustration of semi-variogram models estimates – specimen L, 14 weeks age

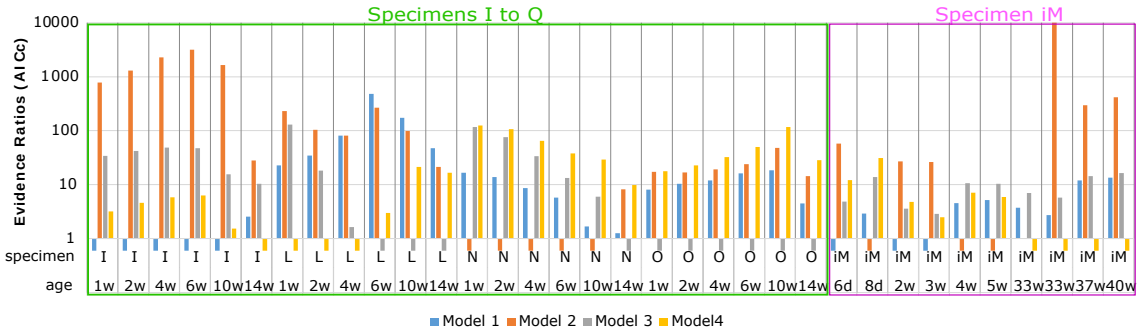

Figure 11. Evidence Ratio comparison of each model for each specimen (log-scale)

https://doi.org/10.26168/ajce.41.4.6

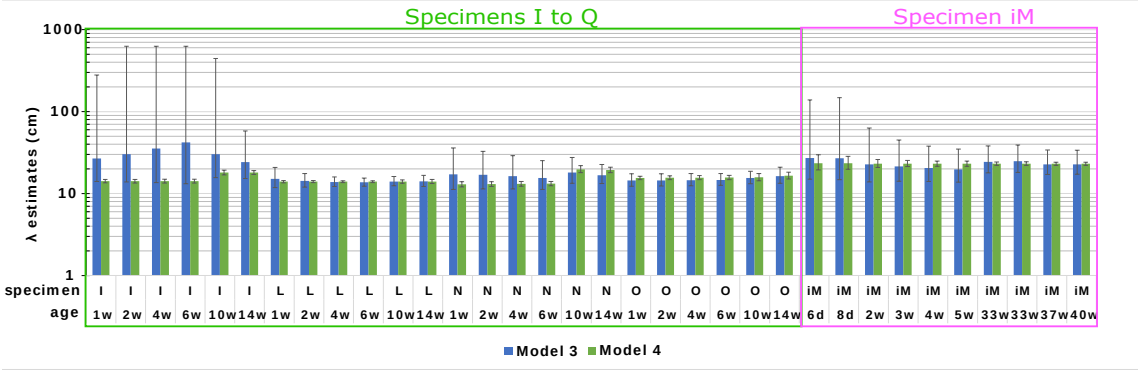

Figure 12. Estimates of wavelength λ of models 3 and 4 for each specimen (log-scale)

B. Estimation of parameters for sets of trajectories

Since CI of fluctuation parameters' estimates merge well for common specimen and depth, we consider these sets of trajectories as realizations of the same RF to take this into account in the estimates and reduce their CIs. Figure 13 shows then the computed ERs, where we see the best fit for both projects are either model 3 or 4. For specimen N, goodness-of-fit of model 1 and model 3 are equivalent and we keep model 3 as we observe hole effect empirically. Thus, we plot the wavelength parameter λ estimates and CIs for each best model on Figure 14. We see then that for specimens I to O, λ falls between 14 cm and 21 cm with very tight CIs, close to the 17.5 cm manually vibration spacing, whereas for specimen iM λ is 23 cm, with a CI ranging from 21 cm to 25 cm, close to the vibration spacing of 29 cm.

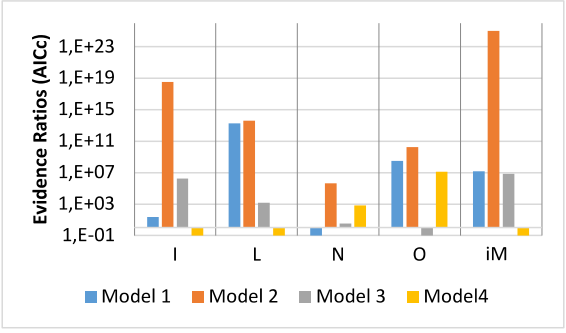

Figure 13 Evidence Ratio comparison of each model for sets of trajectories (log-scale)

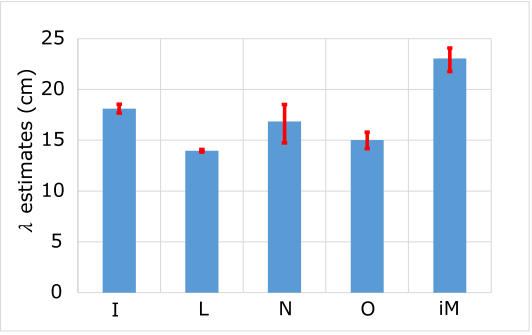

Figure 14 Values and Confidence Intervals of λ from best hole-effect models of both projects

VI. CONCLUSIONS

In this paper, we study the spatial variability of 126 Wenner apparent resistivity trajectories measured on concrete specimens poured with two different vibration protocols in the context of French project SIMAR (9 specimens monitored for 4 months, 1 for 10 months). We especially focus on the evolution of this spatial variability with time, and on its link with vibration protocol. From the work presented in previous sections, we draw conclusions which follow.

(1) Apparent resistivity evolution shows an increase in mean and variance with time for each specimen and depth due to fewer free chlorides during concrete settling and hardening. The deeper layer has lower resistivity compared to the shallow layer. Data in the early age are similar, but in the last six months, there are slight changes that could be influenced by environmental factors.

(2) Empirical spatial variability of apparent resistivity exhibits a significant time-independent spatial signature for common specimen and depth. In particular, significant hole-effect is observed at deeper depth.

(3) Estimation of spatial variability at deeper depth, based on the robust SCAP-1D procedure and considering 4 different semi-variogram models, supports the significance of the empirical observation of hole effect. Indeed, damped cosine and Gaussian-cosine models, which render hole effect, were found to be the best-fit models. It also supports the significance of the spatial signature in two ways: (i) common spatial variability is identified for common specimen and depth, and (ii) estimated wavelength λ of semi-variogram models roughly corresponds to the lag of vibration protocol for both structures. This latter observation suggests the tight link between concrete properties' spatial variability and its vibration protocol, also noticed by (Clerc, 2021, para. VII.2; VII.3) with both chloride content and resistivity spatial variability on an *in-situ* RC beam.

Note that due to the low Wenner electrode spacing values at studied depth (7 mm and 14 mm), our conclusion may also apply to resistivity.

REFERENCES

Burnham, K.P., Anderson, David Ray, Anderson, David Raymond, 2010. Model selection and multimodel inference: a practical information-theoretic approach, 2. ed., ed. Springer, New York, NY.

Chilès, J.-P., Delfiner, P., 2012. Geostatistics: modeling spatial uncertainty, 2. ed. ed, Wiley series in probability and statistics. Wiley, Hoboken, NJ.

Clerc, R., 2021. Sur l'estimation de la variabilié spatiale des paramètres de corrosion et sa necessité pour les plans de maintenance des ouvrages maritimes en béton armé (These de doctorat). Nantes.

Clerc, R., Oumouni, M., Schoefs, F., 2019. SCAP-1D : A Spatial Correlation Assessment Procedure from unidimensional discrete data. Reliab. Eng. Syst. Saf. 191, 106498. https://doi.org/10.1016/j.ress.2019.106498

Cressie, N.A.C., 1991. Statistics for Spatial Data. J. Wiley.

de Smith, M.J., 2018. Statistical Analysis Handbook.

du Plooy, R., Palma Lopes, S., Villain, G., Dérobert, X., 2013. Development of a multi-ring resistivity cell and multi-electrode resistivity probe for investigation of cover concrete condition. NDT E Int. 54, 27–36. https://doi.org/10.1016/j.ndteint.2012.11.007

Kwiatkowski, D., Phillips, P.C.B., Schmidt, P., Shin, Y., 1992. Testing the null hypothesis of stationarity against the alternative of a unit root. J. Eco. 54, 159–178. https://doi.org/10.1016/0304-4076(92)90104-Y

Lecieux, Y., Rozière, E., Gaillard, V., Lupi, C., Leduc, D., Priou, J., Guyard, R., Chevreuil, M., Schoefs, F., 2019. Monitoring of a Reinforced Concrete Wharf Using Structural Health Monitoring System and Material Testing. J. Mar. Sci. Eng. 7, 84. https://doi.org/10.3390/jmse7040084

Priou, J., Lecieux, Y., Chevreuil, M., Gaillard, V., Lupi, C., Leduc, D., Rozière, E., Guyard, R., Schoefs, F., 2019. In situ DC electrical resistivity mapping performed in a reinforced concrete wharf using embedded sensors. Constr. Build. Mater. 211, 244–260. https://doi.org/10.1016/j.conbuildmat.2019.03.152

Pyrcz, M.J., Deutsch, C.V., 2003. The whole story on the hole effect. Geo. Asso. Aus. New. 18, pp.3-5.

Wasserman, L., 2004. All of Statistics, Springer Texts in Statistics. Springer New York, New York, NY. https://doi.org/10.1007/978-0-387-21736-9